Pure Appl. Geophys.
© 2024 The Author(s), under exclusive licence to Springer Nature Switzerland AG
https://doi.org/10.1007/s00024-023-03386-9

Pure and Applied Geophysics

Investigating Multiple Ionospheric Disturbances Associated with the 2020 August 4 Beirut Explosion by Geodetic and Seismological Data

Mohamed Freeshah,[1,2] Erman Şentürk,[3] Xiaohong Zhang,[1] Hamdullah Livaoğlu,[4] Xiaodong Ren,[1] and Nahed Osama[5]

Abstract—In this study, we investigated oscillatory disturbances in the atmosphere [from GNSS-derived ionospheric slant total electron content (STEC)] and in the solid Earth (from triaxial seismic data) following the 4 August 2020 Beirut port explosion in Lebanon. The ionospheric disturbances were investigated under meticulous observations of the space weather indices. The STEC sequences were analyzed by the Savitzky-Golay smoothing filter to check the ionospheric response to the blast. Our results showed that the induced wave structures have significant multiple ionospheric disturbances associated with the explosion epicenter. The research findings showed that the ionosphere responds to the severe blast with two time arrivals. The first time arrival was after the blast within a few minutes and had a low frequency. The second time arrival for the ionospheric disturbance was after > 2 h from the explosion time with high frequency compared with the first one. These ionospheric disturbances were associated with the time and space of the blast. The speed of induced waves in the northern direction of the explosion was slower than the waves in the western and the southern directions, respectively. Finally, the seismological data revealed that there were two major blasts in the Beirut port. The first blast triggered a severe blast after 5 s. Our results are a significant indication that the ionospheric disturbances are influenced by the acoustic gravity wave activity induced by the blast rather than by other random events.

Keywords: Beirut explosion, GNSS, total electron content (TEC), seismic data.

1. Introduction

The investigation of ionospheric perturbations is crucial for communication and navigation systems where the ionosphere is an atmospheric part that has a dispersive medium for electromagnetic signals. However, currently irregular ionospheric variations cannot be predicted or modulated in advance (Freeshah et al., 2020a, 2020b). The irregular ionospheric variations happen because of an abnormal behavior related to one of these events: (1) short-time events such as strong storms, traveling ionospheric disturbances (TIDs), and ionospheric bubbles; (2) space-based events such as solar flares, solar winds, solar eclipse, the Chelyabinsk meteorite, and geomagnetic storm; (3) Earth-based events such as earthquakes, tsunamis, volcanic eruptions, and cyclones; (4) anthropogenic events such as rocket launches and nuclear explosions (Amieri-Simkooei & Asgari, 2012; Chen et al., 2020; Afraimovich et al., 2013; Freeshah et al., 2020a, 2020b, 2021a, 2021b; Jain et al., 1996; Park et al., 2011; Salem et al., 2015; Savastano et al., 2017; Wang et al., 2016; Yu et al., 2015; Zhang & Tang, 2015a, 2015b). The space weather indices such as geomagnetic storms and solar radiations play a dominant role in the ionosphere's dynamic regime (Hargreaves, 1992; Schunk & Sojka, 1997; Sojka et al., 1981). However, many researchers have found that ionospheric disturbances were caused by natural hazards such as earthquakes, tsunamis, volcanic eruptions, and cyclones (Freeshah et al.,

[1] School of Geodesy and Geomatics, Wuhan University, 129 Luoyu Road, Wuhan 430079, China. E-mail: mohamedfreeshah@whu.edu.cn; xhzhang@sgg.whu.edu.cn; xdren@whu.edu.cn

[2] Geomatics Engineering Department, Faculty of Engineering at Shoubra, Benha University, 108 Shoubra St., Cairo 11629, Egypt.

[3] Department of Geomatics Engineering, Kocaeli University, İzmit, Turkey. E-mail: erman.senturk@kocaeli.edu.tr

[4] Department of Geophysical Engineering, Kocaeli University, İzmit, Turkey. E-mail: hlivaoglu@gmail.com

[5] State Key Laboratory of Information Engineering in Surveying, Mapping and Remote Sensing, Wuhan University, 129 Luoyu Road, Wuhan 430079, China. E-mail: nahed.osama@whu.edu.cn

Published online: 20 February 2024

2023). Notably, a few studies deal with the ionospheric perturbations caused by anthropogenic events such as nuclear and and surface explosions (Calais et al., 1998; Dautermann et al., 2009; Fitzgerald & Carlos, 1997).

The infrasonic and gravity waves (IGWs) are associated with powerful natural and anthropogenic explosions that further significantly disturb the ionosphere (Adil et al., 2021). A tremendous blast can perturb the Earth's upper atmosphere. The solid Earth modes could overlap with the atmosphere's principal modes allowing for the triggering of oscillatory acoustic disturbances by Earth excitation events. Atmospheric waves can be classified as infrasonic waves and gravity waves, especially the gravity waves caused by geophysical events, such as underground nuclear explosions (Krasnov & Drobzheva, 2005; Rudenko & Uralov, 1995) and surface explosions (Calais et al., 1998). Consequently, these waves can transfer the energy from the lower atmosphere to the upper atmosphere, which produces ionospheric disturbances based on subsequent interactions with ionospheric plasma. The F layer is the highest region in the ionosphere, located approximately 150 to 600 km above the surface of the earth. F region is divided into two sub-regions, F1 (lower) and F2 (higher). F region has the most significant impact on changes in the total electron concentration. Notably, the ionosphere F layer is highly dynamic and undergoes significant variations on a daily and seasonal basis. It is affected by various parameters such as geomagnetic activity, solar activity, and atmospheric conditions (Knížová et al., 2021; Kutiev et al., 2013). In addition, coronal mass ejections and solar flares can significantly increase the ionization in the F region leading to enhanced electron densities, while solar eclipses can increase their depletion (Şentürk et al., 2021). Therefore, the levels of F region ionization could affect radio signals (e.g., navigation and telecommunication signals) from satellites to receivers depending on the refractive index's variations in the ionosphere. Many researchers have investigated atmospheric coupling based on simulations and real data (Artru et al., 2004; Azeem et al., 2015; Kundu et al., 2021). Some parameters significantly affect the IGWs' vertical propagation such as thermal conditions, temperature variation, viscosity, wind velocity, and wave-to-wave interactions (Mohannakumar, 2008; Vadas & Fritts, 2009). In the higher atmosphere, the IGWs are more susceptible to wind filtering, convective dissipation, and attenuation at the mesosphere layer than internal gravity waves because of the small cut-off frequency and its structure at small spatial scales. In this regard, during dissipation and attenuation processes, momentum and energy are deposited close to the mesosphere layer, resulting in neutral wind's horizontal acceleration, i.e., the thermospheric body force (Vadas & Fritts, 2009).

In 1958, Cullington showed the first results associated with above-ground nuclear tests in Johnston Island, Northern Pacific (Cullington, 1958). Hence, atmospheric waves have been found during the above-ground nuclear test performed by the Soviet Union. As a result, the huge above-ground tests were banned in 1963 and replaced by underground explosions for nuclear tests which cause an atmospheric wave with relatively smaller amplitudes (Latter et al., 1961). Previous studies have used Doppler sounding with time-delayed correlation techniques and sound waves to detect ionospheric oscillations due to surface explosions (Webb & Daniels, 1964). In 1997, GPS-derived TECs were used to determine the propagation speed and duration of wave propagation in the ionosphere during the New Mexico explosion (Fitzgerald, 1997). Researchers have investigated the ionospheric disturbances associated with the 2009 underground nuclear explosion (UNE) in North Korea by using GNSS observations (Park et al., 2011; Zhang & Tang, 2015a, 2015b). They detected induced traveling ionospheric disturbances (TIDs) and estimated the velocity of TIDs through UNE by using GPS dual-frequency data. Meanwhile, Zhang and Tang (2015a, 2015b) concluded different time arrivals for the ionospheric perturbations by tracing the explosion epicenter of the UNE and using the multi-step numerical difference technique. The anthropogenic blasts could be a source of ionospheric disturbances via infrasonic and gravity waves with the neutral atmosphere and ionosphere (Astafyeva, 2019; Komjathy et al., 2016; Meng et al., 2019; Vergados et al., 2020). The potential effects of severe blasts are of considerable interest to researchers such as radio- and

geophysicists. These effects make it possible to reveal the physical mechanisms for transporting the perturbations in horizontal and vertical directions and investigate the reasons for the interaction of the subsystems in the lithosphere-atmosphere-ionosphere system. Nevertheless, sparse investigations are dealing with ionospheric responses to powerful chemical explosions. At 15:08 UTC (Coordinated Universal Time) on 4 August 2020, a massive explosion took place at and destroyed the Beirut port. A giant store of about 2750 tons of ammonium nitrate left in one of the harbor wards was believed to be the substance that was exploded. Consequently, the blast of Beirut port was predicted to cause significant signatures in the ionosphere (Freeshah et al., 2021b, Saqib et al., 2023).

In this study, we analyzed the STEC response to the Beirut explosion on 4 August 2020 through the GNSS-based STEC data. GNSS observations from ground-based International GNSS Service (IGS) stations and Turkey Continuously Operating Reference Stations Network (CORS-TR) in the regions around the blast were used to investigate the variations of the ionosphere. Based on a radio system for sounding the ionosphere, Chernogor and Garmash (2021) detected increases in the phase of the ionospheric wave and the signal amplitude of about 5.3° and 3.3%, respectively, over the explosion in the City of Beirut. Kundu et al. (2021) investigated the ionospheric response to this event at only the southern part of the blast. They stated, "We also note that such clear disturbance signals are either missing or ambiguous at GNSS stations far to the north, e.g., in Turkey and Cyprus." Jonah et al. (2021) investigated the ionospheric response to this event at only the southern part of the blast over 20 GPS stations. Both studies by Jonah et al. (2021) and Kundu et al. (2021) have used the converted vertical TEC (VTEC) to study the ionospheric response to the blast whereas VTEC is a projected value from STEC by using an ionospheric mapping function, and the polynomial fitting could filter out the lower frequency changes (Freeshah et al., 2020a). Meanwhile, we have used a superior approach to detect ionospheric disturbances based on STEC sequences. Also, we have focused on the missing ionospheric response in different directions during the explosion. The steady state of space weather before and during the event indicated that the observed variations of STEC sequences were caused by the giant ammonium-nitrate explosion. We aim to enhance the understanding of the physical mechanism based on studying the seismic data with the ionospheric response. Therefore, we have studied the properties of the explosion such as frequency content and the bomb's monolithic characteristic (one blast or more triggered) in the manner of spectral analysis using wavelet transform based on the available seismological data around the explosion epicenter.

In this paper, we presented data resources such as Beirut explosion information, geomagnetic field and solar-terrestrial environment, IGS, CORS-TR, and seismic data. Then, we presented the methods and analyzed ionospheric variations based on de-trend STEC observations. Finally, the last section presents the conclusions of this study.

2. *Beirut Explosion Information and Datasets*

2.1. *Beirut Explosion Information*

This event is an exceptional anthropogenic event, so we are trying to describe the explosion in as much detail as possible to understand the blast and its mechanisms to perturb the ionosphere. At 15:08 UTC on 4 August 2020, a massive explosion devastated the Beirut port, which is the main seaport in Lebanon. A giant store of ammonium nitrate left in one of the harbor wards was believed to be the substance that exploded. According to Lebanon's Prime Minister Hassan Diab, to trace the statement and the related political crisis, we can refer to (https://www.hrw.org/video-photos/interactive/2021/08/02/lebanon-evidence-implicates-officials-beirut-blast-targeted); about 2750 tons of ammonium nitrate had been unsafely stored at a warehouse in the port, which was the reason for the blast. Ammonium nitrate is not flammable by itself, but as an oxidant, it increases combustion and allows other materials to catch fire more easily. Therefore, it is necessary to adhere to strict rules about its storage, keeping it away from sources of fuel and heat (Jonah et al., 2021; BBC News, 2020; Evening Standard, 2020). In 2022, United Nations experts reported that the Beirut explosion is one of the biggest non-nuclear

explosions recorded, destroying 77,000 apartments, killing 218 people, wounding 7000, leaving 300,000 displaced and at least 80,000 children homeless, and causing about $3.8–4.6 billion in material damage. This explosion caused a cloud of smoke with the famous "mushroom" shape to rise hundreds of meters in the atmosphere over the Beirut Port.

According to the École Supérieure de Physique et de Chimie Industrielles (ESPCI) Institute of Physics in France, the force of the explosion that occurred in the Beirut port is equivalent to that of a "tactical nuclear bomb." According to international journalism, there were two explosions separated by 33 s, not one explosion. The ammonium nitrate materials were distributed over a length of 130 m and width of 40 m in the ward (BBC News, 2020; Evening Standard, 2020). Ammonium nitrate cannot cause an explosion without receiving an explosive shock wave with a temperature of $> 210°$ C; the first explosion occurred in the back of the warehouse, and this was sufficient to prepare the materials for the explosion and to dissolve them to melt into a single mass. Then, after 33 s, a second explosion happened in the middle of the warehouse and the seaside. Figure 1 shows the Beirut port before and after the blast (BBC News, 2020; Evening Standard, 2020).

The flash of blast wave of the second explosion was in the horizontal direction from the wheat silos while a small part of the blast was in the vertical direction. In fractions of a second, negative pressure formed causing a miniature nuclear explosion force of 1.2 terra Joules and a pressure capacity of 210 MPa/m^2. The storming of the explosive wave caused massive damage at a distance of 3 km from the site of the explosion, and its range reached up to 24 km horizontally, while 50% of its strength went towards the sea. Notably, the wheat silos reduced the explosion intensity in the west of Beirut and the airport direction. The explosion was heard in all Lebanese regions. The Jordanian Seismological Observatory recorded that the Beirut explosion equals an earthquake of 4.5 magnitude, while residents of Cyprus, 240 km from Lebanon, felt the explosion according to the Central European Seismological Center. On the other side, the explosion's infrasound was recorded at seismic stations within $\sim$ 500 km of captured seismic waves. In addition, countries such as Tunisia, Germany, and Ivory Coast recorded the



Figure 1
Devastating effects on the Beirut port: left panels show before the blast, right panels show after the blast. Note: the two top panels are not taken from the exact same exposure point

infrasound effect resulting from the event (Pilger et al., 2021). The explosion was a massively destructive force, which some thought was a nuclear bomb, but it was not, according to the Lebanese Atomic Energy Commission.

2.2. Geomagnetic Field and Solar-Terrestrial Environment

Space weather indices represented in geomagnetic activities and solar radiation are the dominant influencers of the ionospheric variations (Afraimovich et al., 2008). In the present study, the disturbance storm-time (D_{st}) and K_p "geomagnetic indices," solar wind speed (V_{sw}), and the solar radio flux $F10.7$ cm "solar indices" were used in the analysis. For the steady-state of the space weather indices, the geomagnetic field intensity should be low (Dst $> -$ 50 nT), where nTs are nano-Tesla, the Kp index is < 4, and solar intensity should be low (F10.7 < 100 sfu), where sfu is solar flux unit: 1 sfu = 10^4 Jy = 10^{-22} W m^{-2} Hz^{-1} = 10^{-19} erg s^{-1} cm^{-2} Hz^{-1}, and the Vsw is low when its value is < 400 km/s (Afraimovich et al., 2008; Şentürk et al., 2021).

2.3. The Turkish Continuously Operating Reference Stations Network (CORS-TR)

The GNSS dataset used in this study was provided by the IGS stations around the study area and CORS-TR with a sampling rate of 30 s. CORS-TR is a project that is funded by "the Scientific and Technological Council of Turkey (TUBITAK)." There are about 158 permanent GNSS stations homogeneously distributed in Turkey, besides the four stations in the "Turkish Republic of Northern Cyprus." The real-time kinematic applications and differential GNSS corrections are computed at the CORS-TR control centers and then are sent to the GNSS users. CORS-TR aims to calculate the precise transformation parameters between the global datum (WGS-84) and a local datum (ED-50) for the whole area of Turkey as well as perform other surveying and geodetic applications (https://www.harita.gov.tr/).

The collected GNSS datasets at each permanent station are sent to certain control centers by ADSL or GPRS/EDGE. Meanwhile, the computed corrections of the real-time kinematic applications are in the RTCM3.1 and CMR transmission formats and transmitted to the users via the GPRS and network transport of RTCM through internet protocol (NTRIP).

2.4. Ground-Based Records of Seismological Data

The Incorporated Research Institutions for Seismology (IRIS) has reported the event as ML 3.3 local magnitude in Afghanistan for the data collected from the nearest available seismic station in the Global Seismographic Network in Kabul, Afghanistan (34.5408° N, 69.0432° E); for more information we can refer to (http://ds.iris.edu/wilber3/find_stations/11282866). Also, the Beirut explosion has been recorded as an earthquake equal to 4.5 magnitude, according to the Jordanian Seismological Observatory. The residents of Cyprus, which is 240 km away from Lebanon, also felt the explosion according to the Central European Seismological Center. The energy yielded during the blast in the near field of the Earth's surface could have generated seismic waves. In this study, we aim to answer the questions related to the properties of the Beirut port explosion such as frequency content and the bomb's monolithic characteristics by spectral analysis using wavelet transform. We analyzed the seismic archived data around the explosion epicenter, which were retrieved from three organizations: T.R. Ministry of Interior Disaster and Emergency Management Presidency (AFAD), IRIS Data Management Center (IRISDMC), and GFZ Seismological Data Archive (GEOFON).

3. Methods of Calculation of STEC and Analysis Algorithms

3.1. Methods of Calculation of STEC

The ionospheric response to the Beirut explosion was analyzed after calculating the STEC ionospheric information. Hence, we derived the STEC sequences between GNSS satellites and receivers along the line of sight. The ionospheric delay in length unit and STEC can be expressed as a function in frequency f where (f_1 = 1575.42 MHz, f_2 = 1227.60 MHz)

(Hofmann-Wellenhof et al., 1992; Ren et al., 2020a, 2020b) through the equation:

$$\mathrm{STEC} = \frac{I \times f^2}{40.31 \times 10^{16}}, \tag{1}$$

where I denotes the ionospheric delay along the line of sight. Meanwhile, the GNSS observations include two L-band frequencies for the carrier phase and pseudo-range. The mechanism of carrier-to-code leveling (CCL) is applied for each continuous arc. The CCL technique is based on the geometry-free (GF) linear combinations of phase and code measurements to calculate the ionosphere information (Alizadeh et al., 2011; Leitinger, 1996). Researchers have proved that the GF combination is more sensitive to ionospheric activity, especially during the rapid modification of radio waves, which is called ionospheric scintillation (Zhang et al., 2014; Ren et al., 2021). The CCL method eliminates the noise of pseudorange; meanwhile, it retains high precision in the carrier-phase (Freeshah et al., 2021a, 2021b; Li et al., 2013). For more details about the method of calculating STEC, we can refer to (). The final CCL algorithm form for the processed ionospheric observable can be expressed through the equation:

$$\begin{aligned} \tilde{L}_{\mathrm{I,arc}} &= L_{\mathrm{I,arc}} - (aa)_{\mathrm{arc}} \\ &= \mathrm{STEC} + B_{\mathrm{r}} + B^{\mathrm{S}} + \left(\varepsilon_{\mathrm{p}}\right)_{\mathrm{arc}} + \varepsilon_{\mathrm{L}}, \end{aligned} \tag{2}$$

where $\tilde{L}_{\mathrm{I,arc}}$denotes the ionospheric observable of carrier phase, which is leveled to the code-delay one, and $L_{\mathrm{I,arc}}$ is the carrier phase ionospheric observable; ε_{p} and ε_{L} indicate the multi-path and noise for the code-delay observations and the measurements of ionospheric carrier phase, respectively. B^{S} and B_{r} are the satellite and the receiver hardware delays of the pseudo-range code, respectively.

3.2. Algorithms Used in the Analysis Process

To remove the constant bias in the STEC time series and the large-scale variations in the STEC series, the Savitzky–Golay smoothing filter (Chen et al., 2020; Savitzky & Golay, 1964; Tang et al., 2018) was used to fit the STEC time series, which can be expressed as

$$\overline{\mathrm{STEC}}(t) = \sum_{i=-m}^{n} a_i \mathrm{STEC}(t+i) \tag{3}$$

where $\overline{\mathrm{STEC}}(t)$ denotes the fitted STEC at epoch t; $m = 60$ and $n = 60$ are the number of points before and following the data point at epoch t, respectively; the length of the moving window or the temporal sampling of the points is 121 $(m + n + 1)$; a_i expresses the filter coefficient. After fitting the STEC sequence with Savitzky-Golay smoothing filter, the dSTEC time-series sequence can be obtained by subtracting fitted STEC sequences from the observed ones as follows:

$$\mathrm{dSTEC}(t) = \mathrm{STEC}(t) - \overline{\mathrm{STEC}}(t) \tag{4}$$

where $\mathrm{dSTEC}(t)$ is the dSTEC at epoch t. Most frequently, the 3-dB cut-off frequency is chosen as a boundary in a filter's frequency response (Schafer, 2011). After using the Savitzky-Golay smoothing filter, the Morlet wavelet filter is employed to convert the time domain to the frequency domain to detect the ionospheric disturbances of the de-trended STEC sequences.

Eventually, the seismological stations that recorded the blast event have been analyzed according to the signal-noise ratio (SNR) above the two spectral analyses. Then, we filtered the data without distorting the frequency content of the signals performing band bass (0.1–20 Hz) Butterworth digital filter and the order of 2 ($n = 2$).

4. Results and Discussion

4.1. Geomagnetic Field and Solar-Terrestrial Environment

As we know, ionospheric variations are mainly influenced by geomagnetic conditions and solar activity. Therefore, it is of great importance to consider the effect of geomagnetic and solar activity in this study by checking the space weather indices. The meticulous observation of space weather indices shows that the solar and geomagnetic activities were in a steady state. As seen in Fig. 2, during the whole period, no evidence of strong solar activity or geomagnetic activity was observed. The upper panel of Fig. 2 shows the Dst index ranging between + 20

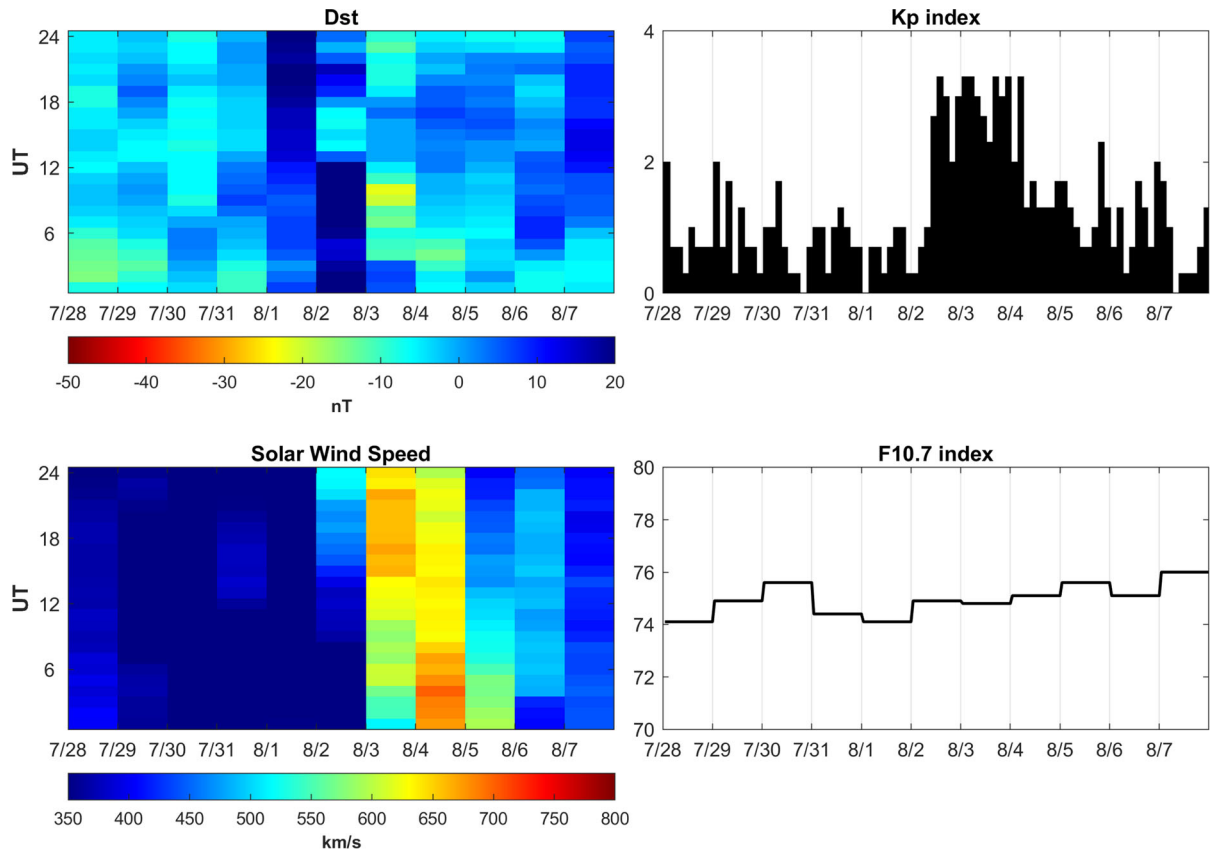

Figure 2
Dst, Kp, Vsw, and F10.7 indices in the period from 28 July 2020 (DOY 210) to 7 August 2020 (DOY 220)

and $-$ 20 nT and K_p index < 4 before, during, and after the blast, which indicates the geomagnetic activity in the steady state for the period of the data.

In the lower panel of Fig. 2, the V_{sw} and $F10.7$ indices indicate that there was a modest level of solar activity during the explosion because Vsw was around 600 km/s and $F10.7$ values were < 100 sfu. Figure 2 indicates that the solar radiation and geomagnetic activity components were relatively stable for days before, during, and after the Beirut explosion. It is probable that the ionospheric conditions during the blast using the Savitzky–Golay filter and Morlet wavelet were not contributed by solar and geomagnetic activities; the results of these methods will be shown later in the next section.

4.2. *Ionospheric Disturbances During the Beirut Explosion*

The Beirut blast occurred close to sunset according to Lebanese local time; fortunately, at the longitude of Beirut, the equatorial plasma bubble production rate is not high at this time of year. Therefore, detection level of the potential ionosphere response to the blast was very high (Cahyadi & Heki, 2015; Panda et al., 2019). We derived STEC values through GNSS observations from IGS and CORS-TR stations to display the ionospheric response to the blast in Beirut port. The STEC time series over the Beirut port explosion for the day of the event was analyzed by the Savitzky-Golay smoothing filter. The Morlet wavelet filter was employed to convert the time domain to the frequency domain to detect

ionospheric disturbances for the de-trended STEC sequences. To discover the STEC variations, the STEC sequences of IGS stations and CORS-TR stations were utilized to detect the STEC ionospheric variations. By investigating the available satellites during the Beirut blast, we found that satellite G22 was the closest satellite to the blast epicenter. In addition, G22 satellite has the longest continuous arcs, which were started before the blast and were continued for a few hours after the event. Figure 3 shows the spatial distribution of the used IGS, CORS-TR stations, seismic stations, and Beirut port epicenter.

The media reports showed a shock wave erupting from the Beirut explosion at 15:08 UTC on 4 August 2020 (DOY 217) (BBC News, 2020; Evening Standard, 2020). To investigate the ionospheric response and blast-induced wave signature in the ionosphere, we analyzed all the IGS and CORS-TR stations around the Beirut blast. The research findings showed that the ionosphere responds to the severe blast with two time arrivals. The first time arrival was after the blast within a few minutes and had a low frequency, consistent with the results by Jonah et al. (2021) and Kundu et al. (2021). Meanwhile, the second time arrival for the ionospheric disturbance was after > 2 h from the explosion time with higher frequency than that of the first one. Disturbance series extracted by the Savitzky-Golay Filter method from stations DIPK, NICO, and MGOS are presented in Fig. 4. The corresponding Morlet wavelet (middle panels) was used to convert the time domain to frequency domain for de-trended STEC sequences, and satellite ground track included IPPs (right panels). As seen from Fig. 4 (left panel), the first and second ionospheric responses are detected over the stations DIPK, NICO, and MGOS to the north and northwest

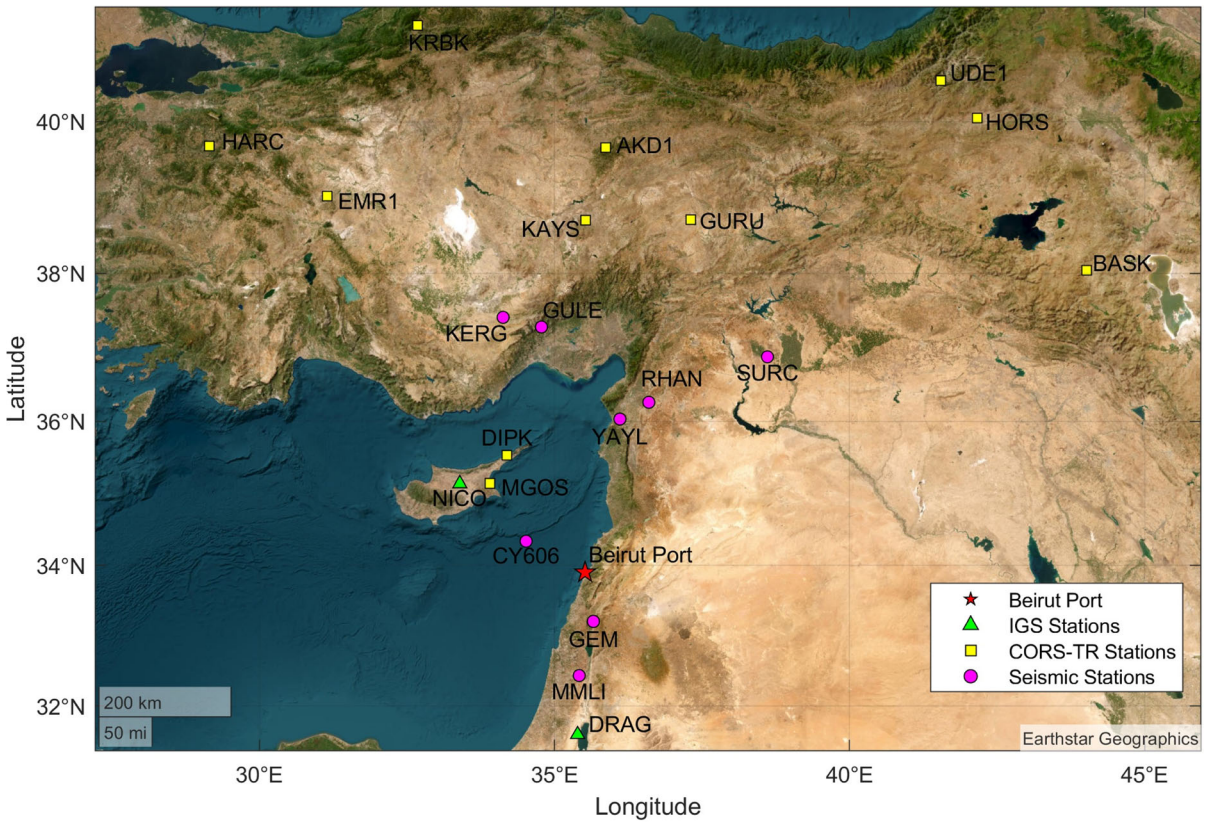

Figure 3
Spatial distribution of the used IGS, CORS-TR, and seismic stations as well as the location of Beirut port

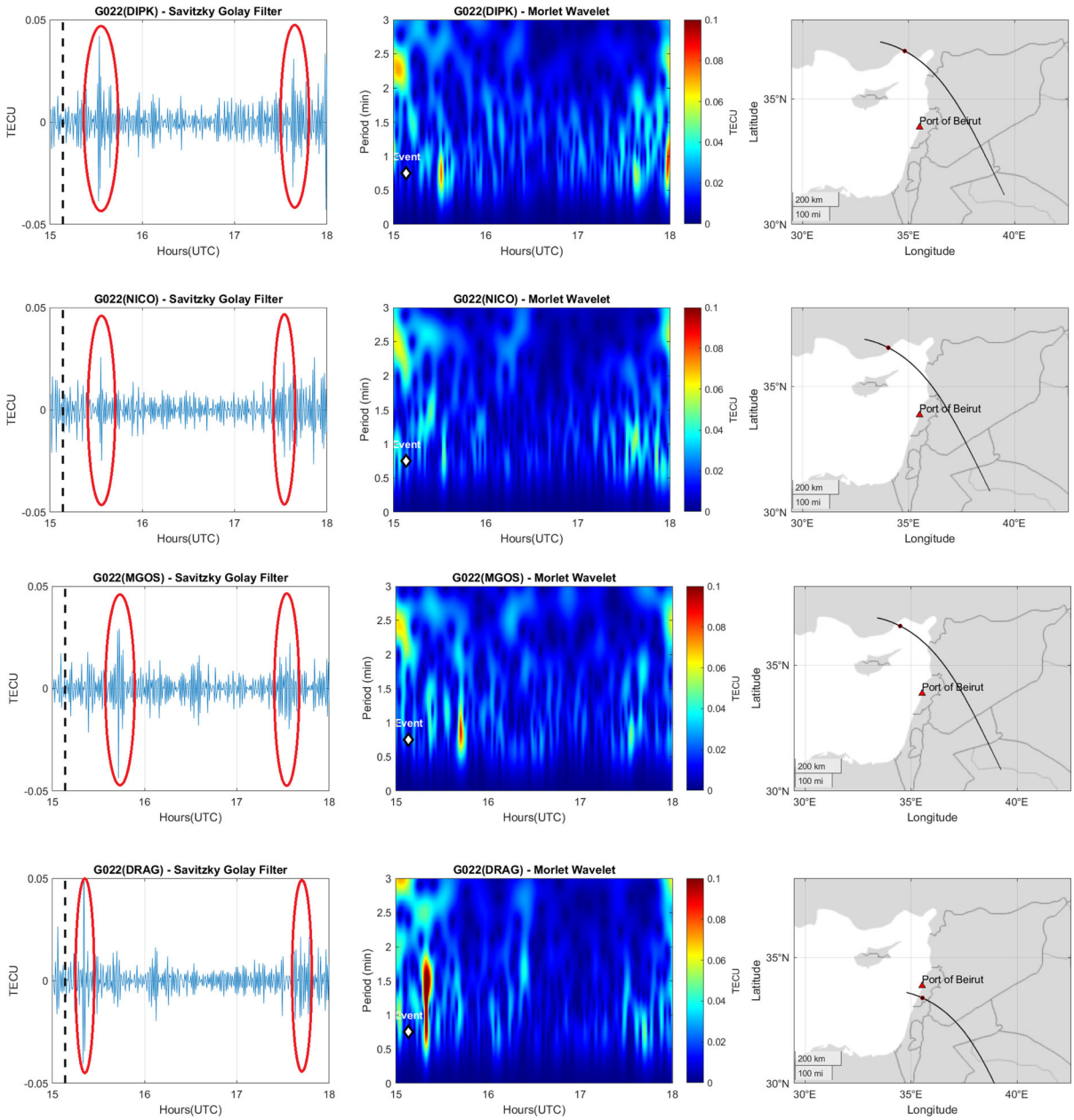

Figure 4

STEC disturbances by Savitzky-Golay filter (left panel), corresponding Morlet wavelet (middle panel), and right panel represent satellite ground track including IPP's location of maximum ionospheric effect (red circle) to the location of Beirut port (red triangle) obtained by GNSS observations of satellite G22 at stations DIPK, NICO, MGOS, and DRAG for the day of the event (DOY 217); the STEC disturbance to the north of the explosion

of the blast in addition to station DRAG in the southern direction of the blast.

Notably, the first-time arrival of ionospheric response coincides with the results of Jonah et al., (2021) and Kundu et al., (2021), whereas the second time arrival is discovered for the first time to our knowledge in this research. The ionospheric disturbances over DIPK, NICO, and MGOS stations are

almost synchronized, especially the second time arrival; the maximum amplitude of the ionospheric response is consistent over the three stations, which could be interpreted by the stations located in the same direction. Besides, the Euclidean distances from the blast epicenter to IPP of maximum amplitude are close each other at about 565.4, 556.8, and 548.9 km for DIPK, NICO, and MGOS stations, respectively. On the other hand, the first-time arrival over DRAG station is detected earlier than at DIPK, NICO, and MGOS stations where the satellite ground track of IPPs over DRAG is closer to the blast. Also, the IPPs over DRAG are located in the southern direction of Beirut port where from one region to another the ionospheric disturbances can travel with different velocities in different regions (Jonah et al., 2018).

To interpret the two time arrivals of the ionospheric response to the Beirut blast, we have to focus on the behavior of these kinds of explosions and understand their physical mechanisms during severe explosions. As a result of the severe blast, atmospheric acoustic waves can be one of two waves: First, infrasonic waves occur if the frequencies are low enough, and ionospheric influence will appear after a few minutes from the blast; this effect coincides with the first time arrival of ionospheric disturbances associated with the blast. Second, gravity waves are associated with surface explosions (Calais et al., 1998) as a geophysical event can be of such origins and disturb the ionosphere. The behavior of ionospheric disturbance in the case of gravity waves is long lasting for a few hours after the geophysical event, and the disturbance frequency is lower than that of the infrasonic waves. In addition, the infected area around the event is much larger so the effect of gravity waves on the ionosphere extended for long distances from the blast epicenter; likely the second time arrival is infected by gravity waves induced by the Beirut blast.

More investigations have been done over several stations that are quite far from the blast to detect the potential second-type effect of ionospheric disturbances associated with the gravity waves generated by the Beirut blast. As seen in Fig. 5, the stations HARC, UDE1, KRBK, AKD1, BASK, EMR1, GURU, HORS, and KAYS from CORS-TR have ionospheric disturbances more than 2 h after the severe blast. Table 1 shows the delays between the explosion time and time of first and second ionospheric STEC disturbances. Since the stations are located far from the blast epicenter, the first time arrival has not been detected over the stations HARC, UDE1, KRBK, AKD1, BASK, EMR1, GURU, HORS, and KAYS, whereas the second time arrivals are detected over the aforementioned stations. We found ionospheric disturbances in the north, east, and northeast directions about 2 h after the blast. The left panel shows the STEC disturbances by Savitzky-Golay filter, and the dashed line represents the explosion time. The middle panel shows the corresponding Morlet wavelet filter to convert the time domain to frequency domain for de-trended STEC sequences. The right panel displays the satellite ground track of the included IPPs. The IPP location of the maximum ionospheric effect (red circle) at the location of Beirut port (red triangle) was obtained by GNSS observations of the G22 satellite. These results agree and are synchronized with the second time arrival in Fig. 4.

Figure 5 ▶
STEC disturbances by Savitzky-Golay filter (left panel), corresponding Morlet wavelet (middle panel), and right panel represents satellite ground track including IPP's location of maximum ionospheric effect (red circle) to the location of Beirut port (red triangle) obtained by GNSS observations of satellite G22 at stations HARC, UDE1, KRBK, AKD1, BASK, EMR1, GURU, HORS, and KAYS for the day of the event (DOY 217); the STEC disturbance to the north of the explosion

Notably, the relationship between electron density fluctuations and the frequency of dynamic disturbances could be complicated, and it is impacted by several parameters such as wave characteristics, the ionospheric background, and the solar and geomagnetic activities. The research results show that there are two kinds of perturbations in the ionospheric STEC sequences: low-frequency ionospheric perturbations after a few minutes were detected over four stations (near the epicenter, Figs. 3 and 4), and high-frequency waves after > 2 h, were detected over 13 stations (Table 1). Two scenarios can interpret these two kinds of STEC disturbances. In the first scenario, the multiple ionospheric disturbances can be attributed to the infrasonic waves in the lower and higher

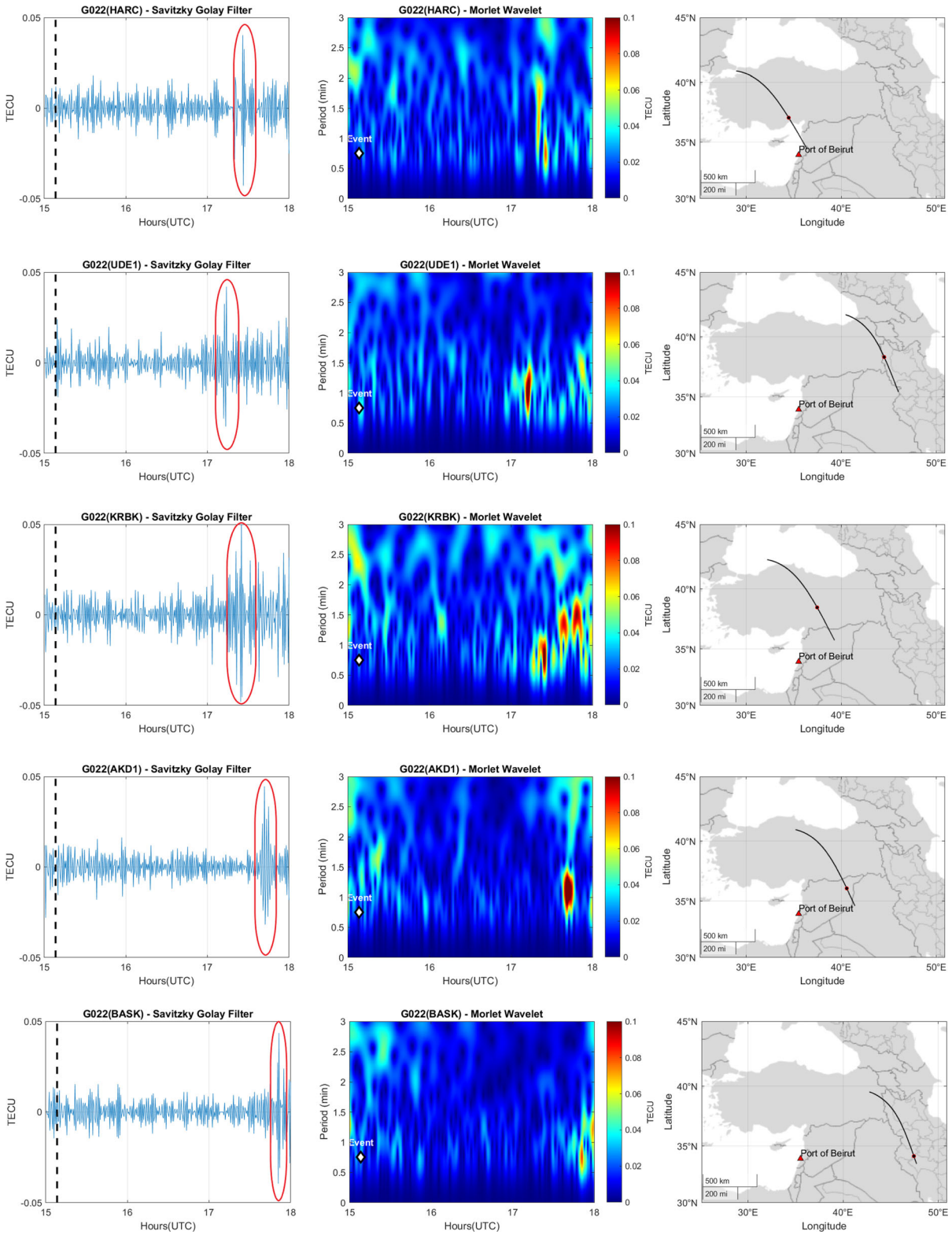
G022(HARC) - Savitzky Golay Filter
G022(HARC) - Morlet Wavelet
G022(UDE1) - Savitzky Golay Filter
G022(UDE1) - Morlet Wavelet
G022(KRBK) - Savitzky Golay Filter
G022(KRBK) - Morlet Wavelet
G022(AKD1) - Savitzky Golay Filter
G022(AKD1) - Morlet Wavelet
G022(BASK) - Savitzky Golay Filter
G022(BASK) - Morlet Wavelet
TECU
Hours(UTC)
Period (min)
Event
Latitude
Longitude
Port of Beirut
500 km
200 mi

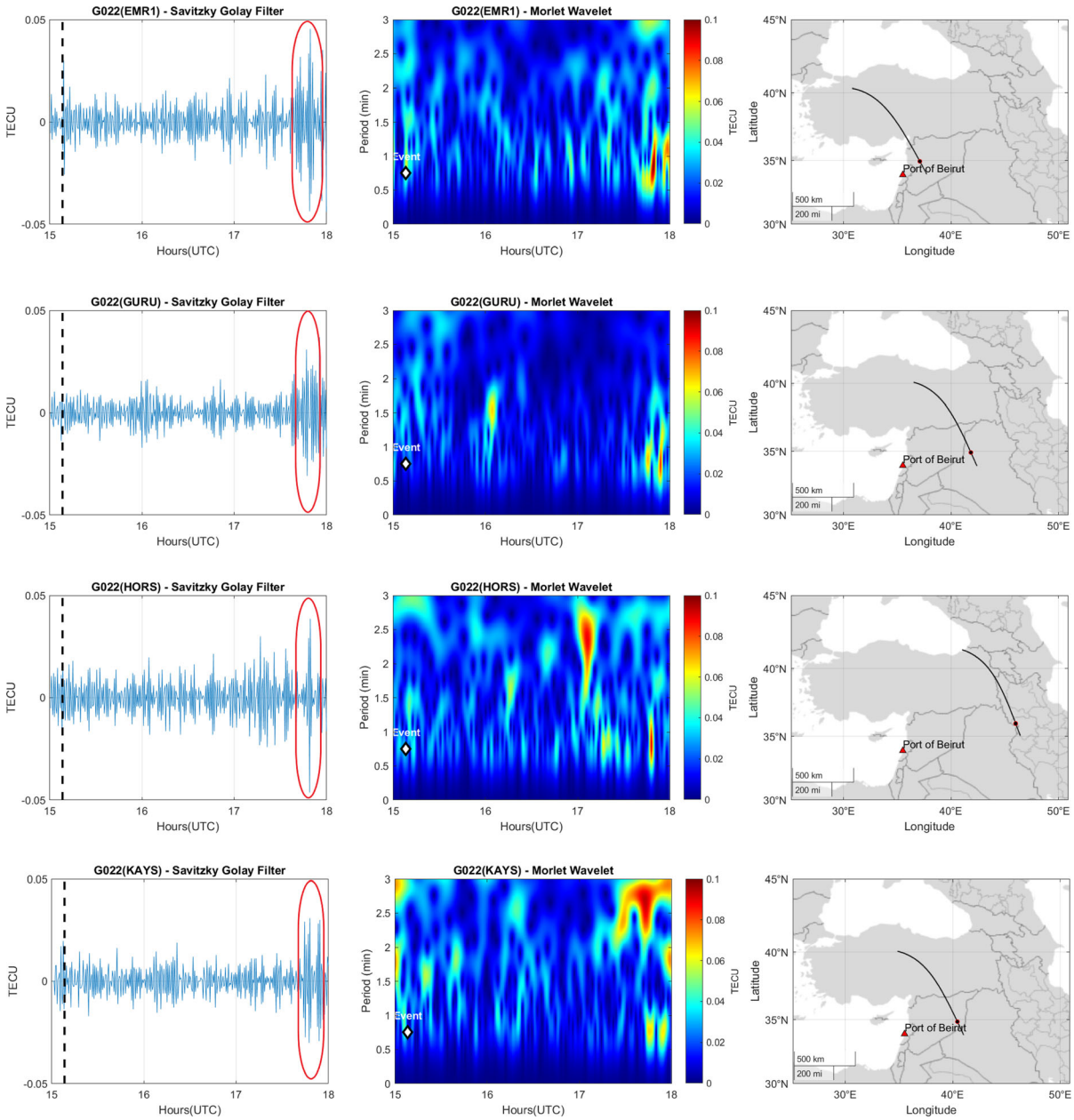

Figure 5
continued

ionosphere. However, this scenario is not recommended because if we consider only the infrasonic waves, then the lower the ionosphere, the higher the frequency, and vice versa (Zhang & Tang, 2015a, 2015b). In the second scenario, the interpretation that we adopt here according to the amplitudes, periods, and average propagation velocities, infrasonic waves cause the first STEC disturbance after a few minutes over the four stations DIPK, NICO, MGOS, and DRAG (close to blast epicenter) if the frequencies are low enough, and ionospheric influence will appear after a few minutes from the blast; this effect coincides with the first-time arrival of ionospheric disturbances associated with the blast.

Table 1

Time delays between the explosion time and time of first and second delays of STEC disturbances

Station name	Time of first delay of disturbance (min)	Time of second delay of disturbance (min)
DIPK	19.0	148.0
NICO	21.5	134.5
MGOS	22.0	133.5
DRAG	10.5	148.0
HARC	Ambiguous	136.5
UDE1	Ambiguous	122.0
KRBK	Ambiguous	129.0
AKD1	Ambiguous	139.5
BASK	Ambiguous	139.0
EMR1	Ambiguous	141.0
GURU	Ambiguous	148.0
HORS	Ambiguous	155.0
KAYS	Ambiguous	154.5

The effect of infrasonic waves happened over short distances over the nearest four stations around the blast, and this is consistent with the effect of infrasonic waves, which has a limited range of influence, whereas the second-time arrival could be considered because of internal gravity waves where its range extends for longer distances than that of infrasonic waves, and this is clear for the rest of the stations (Figs. 3 and 5). Other evidence supports this recommendation that the infrasonic waves effect arrives faster than the impact of internal gravity waves, and this coincides with their apparent velocities in the ionosphere. The apparent velocity ranges from $\sim$ 0.8 km/s (infrasonic waves) to 0.2–0.3 km/s (internal gravity wave often excited by very large earthquakes) (Kundu et al., 2021).

The limited number of GNSS satellites affected by the Beirut blast had detectable ionospheric disturbances that interacted with the event for one of the following reasons: (1) at the time of the explosion the satellites did not have good distribution, (2) the electron motion limitation, and (3) the satellite's LOS could be far away from the disturbed ionosphere part or the satellite passed before the effect of the explosion-induced waves or after the electron reionization (Freeshah et al., 2020a; Kundu et al., 2021).

The results in the southern direction of the blast also agreed with the previous studies by Jonah et al. (2021) and Kundu et al. (2021) who studied the ionospheric disturbances over the southern part of the explosion. According to Figs. 4 and 5, significant ionospheric anomalies were associated with the time and space of the blast, and the deviations over some stations had happened a few minutes earlier than at the other stations. This behavior could be attributed to the following reasons. First, we believe that the closer the distance to the intensification ionospheric area, the sooner the disturbances will occur. Second, the ionospheric disturbances have traveled faster in one direction than the other; this assumption was suggested by Jonah et al. (2018). They concluded that from one region to another the velocity of the ionospheric disturbances can travel with different velocities in different regions according to Jonah et al. (2018). Our investigation outcomes regarding the Beirut explosion event showed that the point of maximum ionospheric disturbance in the southern direction was closer to the explosion epicenter, and the speed of the IGWs in the southern direction of the blast was faster than in the western and northern directions. The speed of induced waves in the northern direction of the explosion was slower than that of the western and the southern directions.

Our results regarding the Beirut explosion event are also in good agreement with the previous studies by Jonah et al. (2021) and Kundu et al. (2021). They agreed on the short time taken for the signal to arrive at different IPPs in the ionosphere within a few minutes after the explosion and the other properties of wave propagation such as amplitude, wave frequency, and directivity. The findings acquired from our study provide multiple ionospheric disturbances over stations DIPK, NICO, MGOS, and DRAG; this is an opportunity to understand the impact of the Beirut blast on the ionospheric variation and to endorse the other theoretical and modeling studies on TEC responses to the massive explosions. The synchronization of the ionospheric variations over the IGS stations and the CORS-TR stations over the analyzed directions of the blast indicates that they were induced by the blast rather than by other random events. The results showed that there were ionospheric variations with different strengths and periods.

We suggest that the IGWs generated through the explosion time are the reason for the detected ionospheric disturbances over the GNSS ground-

based stations on the day of the event (DOY 217) for the first time arrival. These results agree with a previous study by Park et al. (2011) which studied the 25 May 2009 North Korean underground nuclear explosion and reported that there are similar short-lived wave oscillations within 23 min after the event. Also, the spectrum period of the ionospheric disturbance over the Beirut explosion almost agreed with another study over the North Korean underground nuclear explosion where they concluded that the high-frequency ionospheric disturbances were detected in a period of approximately 1–2 min (Zhang & Tang, 2015a, 2015b).

The two time arrivals agree with previous studies indicating that severe explosions could perturb the ionosphere with multiple disturbances; even the study of the North Korean underground nuclear explosion (Zhang & Tang, 2015a, 2015b) concluded that there are two types of disturbances in the ionospheric disturbance series, high and low frequency. The study by Astafyeva et al. (2022) noted that the TEC variations show multiple large peaks occurred for tens of minutes over the 15 January 2022 Hunga Tonga explosion.

The ionospheric disturbances close to the explosion epicenter have larger propagation velocities than ionospheric disturbances away from the explosion epicenter, indicating that the propagation velocities feature distance-dependent attenuation. This phenomenon agrees with the view that these ionospheric disturbances are related to the IGWs induced by the Beirut blast. Another reason supporting why the southern sides of the explosion epicenter have significantly faster propagation velocities than the northern parts is because the northward-propagating disturbances are sensitive to the effects of magnetic fields of the Earth (Zhang & Tang, 2015a, 2015b; Cahyadi et al., 2021). There is another potential reason for the multiple time arrivals of ionospheric disturbances induced by the blast. Multiple ionospheric perturbations could be induced by multiple major explosions during the event (Astafyeva et al., 2022). Therefore, we took refuge in the ground-based seismic records and spectral analysis of the explosion to investigate the potential major explosions that may have been caused during the Beirut blast.

4.3. *Ground-Based Seismic Records and Spectral Analysis of the Explosion*

The energy that is yielded during an explosion in the near field of the Earth's surface can generate seismic waves. The recorded seismic waves at regional distances carry important information about the possible source(s) of the sudden energy release (Kurtuluş et al., 2018). In this section, we answer the questions related to the properties of the Beirut explosion, such as frequency content and the bomb's monolithic characteristics in the manner of spectral analysis using wavelet transform. Regarding the spectral analyses, we searched for the stations that have detected the event, and we analyzed them according to the SNR above the value of two spectral analyses. The list of stations analyzed is shown in Table 2.

In Table 2, the stations' sources are the AFAD, IRISDMC, and GEOFON. The signals were detected in the stations with broad-band velocity-based sensors. After the SNR elimination criteria, we filtered the data without distorting the frequency content of the signals by performing a bandpass Butterworth filter with an order of 2 ($n = 2$). We especially searched for the infrasound frequency content < 20 Hz that characterizes such explosions. The raw and the filtered signals can be seen in Fig. 6.

In Fig. 6, the sensors detected the attenuated waves in horizontal components instead of vertical components. Naturally, the explosion generates shock waves and propagates horizontally hundreds of kilometers away. When the distance increases, the vertical components can be amplified because of the

Table 2

Stations and distances from the explosion epicenter

Station	Source	Latitude	Longitude	Distance (km)
GEM	GEOFON	33.21	35.66	77.98
CY606	IRISDMC	34.34	34.52	103.91
MMLI	GEOFON	32.44	35.42	162.97
YAYL	AFAD	36.03	36.11	243.15
RHAN	AFAD	36.26	36.6	280.11
GULE	AFAD	37.28	34.78	382.04
KERG	AFAD	37.41	34.13	410.42
SURC	AFAD	36.88	38.61	433.88

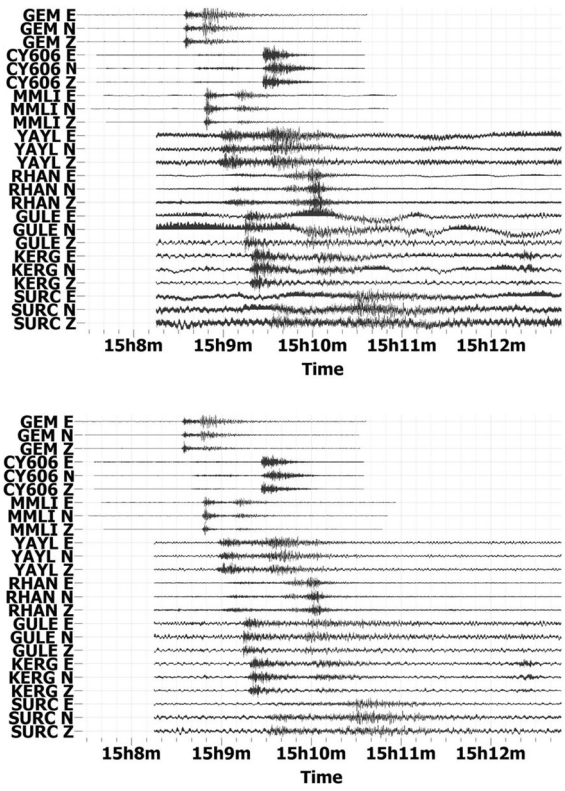

Figure 6
Comparison of raw (upper panel) and filtered (bottom panel) seismological data

site effects (see Fig. 6 SURC station). The waves interfere with the ground generating various bands of frequencies, and the filtering process helps us to determine the interacted ones. The significant anomalies here can be seen in the CY606 station located on Cyprus Island. Although it is located far away from the MMLI station located in Israel, the body waves arrived late at the station because of the possible deceleration effect of the sea on the primer phase of the body waves.

In time-frequency analyses, continuous mother wavelet transforms were used in the predominant amplitude components to reveal the accurate resonant frequencies (Roueff et al., 2004). The mother wavelet parameters were performed carefully for the optimum frequency-time resolution. Continuous mother wavelet transform analysis indicated that the energy releases focused on the moderate frequencies ranging between 0.8 and 10 Hz, which involves infrasound at < 20 Hz (Fig. 7). The recorded E–W component of station GEM shows the fundamental peak frequency as three maximum amplitudes corresponding to the released energy. The first two amplitudes are at 1.2- and 1.5-Hz for a short time of about 20 ms, while the third blast depicts 1.8 Hz after 5 s. This situation shows that there are two major blasts in the port store; one of the blasts triggered another major one after 5 s of the first explosion. At the farther stations, the monotonic energy release was not seen depicting more energy at higher frequencies as a result of messier body-surface wave interference including infrasound characteristic of shock wave codes. These results reinforce the hypothesis that described the Beirut port explosion as one of the most severe nonnuclear humanmade blasts in history with an estimated equivalent yield of 1500 tons of TNT (BBC News, 2020; Evening Standard, 2020). Eventually, the research outcomes confirm that the ionospheric variations were produced by Beirut blast-induced gravity waves rather than by other random events.

5. *Conclusions*

In this study, we investigated the potential ionospheric disturbances due to the Beirut port explosion on 4 August 2020 (DOY 217) over a mid-latitude region. During the underlying Beirut explosion, the enhanced GNSS-STEC variations were observed from several IGS and CORS-TR stations over the area of interest on the day of the event. To verify that the STEC disturbances are not associated with space weather, the D_{st}, V_{sw}, K_p, and $F10.7$ indices were investigated before, during, and after the explosion. The steady state of the space weather before and during the event indicated that the observed variations of TEC sequences were caused by the ammonium nitrate explosion. We have focused on the missing ionospheric response in the northern part during the explosion based on STEC sequences to cover the gap in the recent studies by Kundu et al. (2021) and Jonah et al. (2021). Our investigation outcomes in the southern direction of the Beirut explosion are in good agreement with the aforementioned previous studies, besides the consistency in the short time taken for the signal to arrive at different IPPs, in addition to the agreement in amplitude, wave

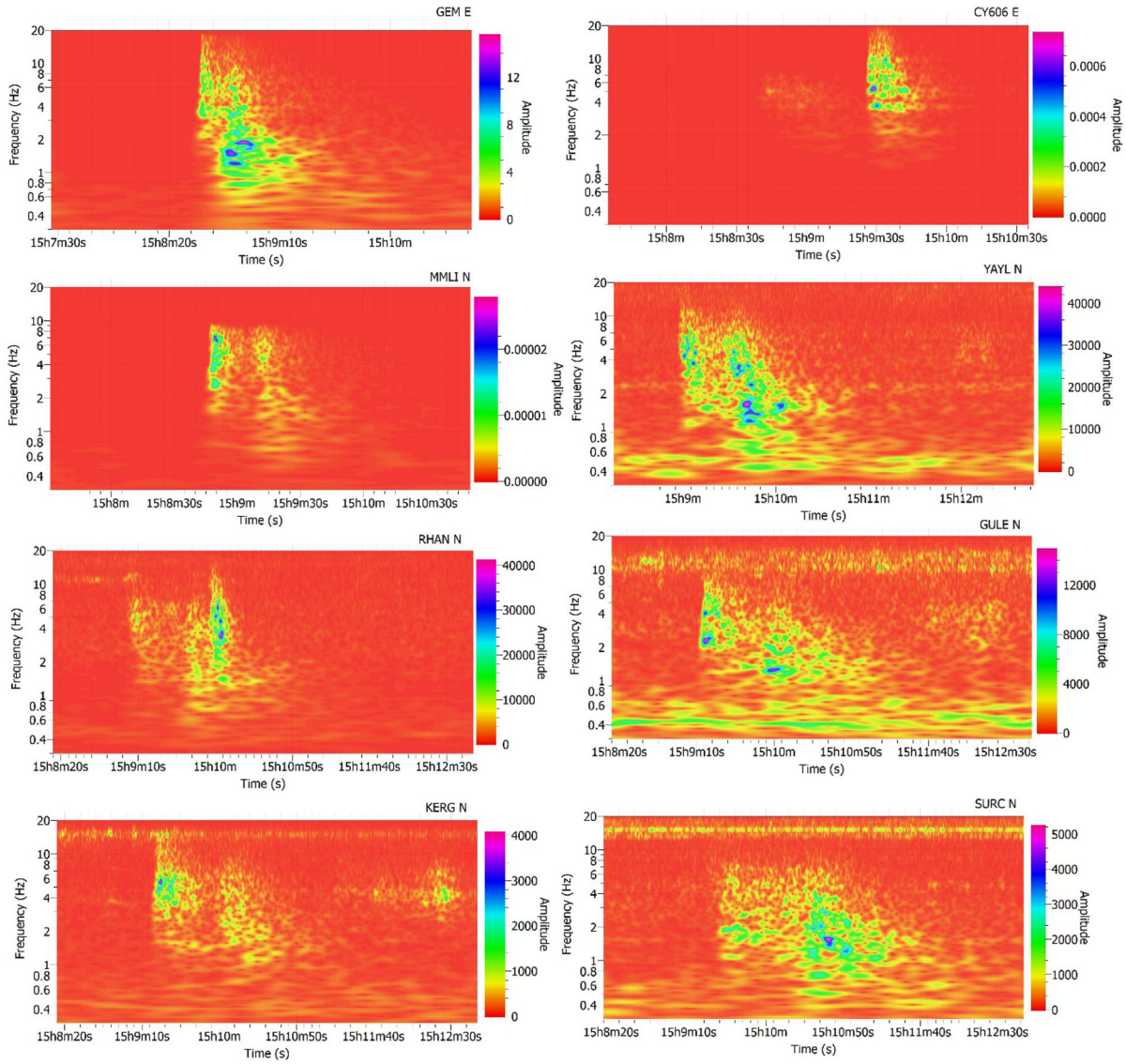

Figure 7

Time-frequency analyses of the recorded signals originating from the explosion. The frequency in Hz and the amplitude of the spectrum depend on the source and propagation path. The Eastern component of GEM (top left) and CY606 (top right) stations and the northern component of other stations were demonstrated. The color bars are at different scales to match the station data, and the *x*-axes (time) are slightly shifted

frequency, and directivity. As a new contribution, our results detected ionospheric disturbances in the northern and the western directions of the blast epicenter. In terms of TECU, our results show that the STEC ionospheric disturbances coincided with the Beirut explosion in space and time, considering a temporal delay for the travel time of wave propagation to disturb the ionosphere. The induced waves of the blast in the southern direction of the blast had the fastest apparent velocity, while in the northern direction, the induced waves had the slowest apparent velocity; this could be because the northward-propagating disturbances are sensitive to the effects of Earth's magnetic fields (Rolland et al., 2011). While the results in this study fit well with the ionospheric disturbances from other resources such as natural

hazards, these waves are characterized by short-lived time within a few minutes. These types of short-lived waves are similar to the observed waves associated with underground nuclear tests (e.g., Park et al., 2011; Zhang & Tang, 2015a, 2015b). Hence, the special characteristic of blasts can lead us to distinguish them from other sources of wave disturbances such as regular ionospheric perturbations. As a new contribution, our research results showed multiple ionospheric disturbances where the second time arrival for the ionospheric disturbance was after > 2 h from the explosion time with high frequency compared with that of the first one. Also, we investigated the seismology data around the anthropogenic explosion. The meticulous observations of the space weather showed that the solar-terrestrial environment and geomagnetic storm indices were in a steady state. Consequently, the synchronization in the ionospheric variations over the IGS and CORS-TR stations indicated that the ionospheric disturbances were induced by the blast rather than by other random events.

Acknowledgements

This work was funded by the National Natural Science Foundation of China Research Fund for International Young Scientists (Grant no. 42250410331), the National Natural Science Foundation of China (no. 42174031, no. 42230104). The numerical calculations have been done on the supercomputing system in the Supercomputing Center of Wuhan University, Wuhan, China. The authors are very grateful to CORS-TR and IGS data for providing GNSS data, NASA for providing space weather indices. The triaxial seismic data from the Incorporated Research Institutions for Seismology (IRIS), T.R. Ministry of Interior Disaster and Emergency Management Presidency (AFAD), IRIS Data Management Center (IRISDMC), and GFZ Seismological Data Archive (GEOFON). We also gratefully acknowledge the MATrix LABoratory (MATLAB) software (https://matlab.mathworks.com/).

Author Contributions Conceptualization, MF; Data curation, MF, HL, and XR; Formal analysis, EŞ, NO, and MF; Funding acquisition, MF, XR, and XZ; Investigation, MF, HL, and EŞ; Methodology, MF; Project administration, XZ and XR; Resources, MF and N O; Software, MF, EŞ, and HL; Supervision, XZ; Validation, MF, XR, and NO; Visualization, MF, EŞ, and NO; Writing—original draft, MF; Writing—review and editing, MF, XZ, EŞ, NO, and XR All authors have read and agreed to the published version of the manuscript.

Data availability

We uploaded the raw data of CORS-TR at https://zenodo.org/record/5656281#.YYoreWBBw2w and IGS data is open access on (https://igs.org/data/), space weather indices available at (https://omniweb.gsfc.nasa.gov/form/dx1.html). The triaxial seismic data from the Incorporated Research Institutions for Seismology (IRIS), T.R. Ministry of Interior Disaster and Emergency Management Presidency (AFAD), IRIS Data Management Center (IRISDMC), and GFZ Seismological Data Archive (GEOFON), all seismic data used in this study is available at (https://zenodo.org/record/5656281#.YYoreWBBw2w). The data presented in this study are available on request from the first author or on the corresponding websites.

Declarations

Conflict of interest The authors declare no competing interests.

Publisher's Note Springer Nature remains neutral with regard to jurisdictional claims in published maps and institutional affiliations.

Springer Nature or its licensor (e.g. a society or other partner) holds exclusive rights to this article under a publishing agreement with the author(s) or other rightsholder(s); author self-archiving of the accepted manuscript version of this article is solely governed by the terms of such publishing agreement and applicable law.

References

Adil, M. A., Şentürk, E., Pulinets, S. A., & Amory-Mazaudier, C. (2021). A lithosphere–atmosphere–ionosphere coupling phenomenon observed before M 7.7 Jamaica earthquake. *Pure and Applied Geophysics, 178*, 3869–3886. https://doi.org/10.1007/s00024-021-02867-z

Afraimovich, E. L., Voeykov, S. V., Ishin, A. B., Perevalova, N. P., & Ruzhin, Y. Y. (2008). Variations in the total electron content

during the powerful typhoon of August 5–11, 2006, near the Southeastern Coast of China. *Geomagnetism and Aeronomy, 48*(5), 674–679. https://doi.org/10.1134/s0016793208050113

Afraimovich, E. L., Astafyeva, E. I., Demyanov, V. V., Edemskiy, I. K., Gavrilyuk, N. S., Ishin, A. B., Kosogorov, E. A. et al. (2013) A review of GPS/GLONASS studies of the ionospheric response to natural and anthropogenic processes and phenomena. *Journal of Space Weather and Space Climate*, 3. https://doi.org/10.1051/swsc/2013049

Alizadeh, M. M., Schuh, H., Todorova, S., & Schmidt, M. (2011). Global ionosphere maps of VTEC from GNSS, satellite altimetry, and Formosat-3/COSMIC data. *Journal of Geodesy, 85*(12), 975–987.

Amieri-Simkooei, A. R., & Asgari, J. (2012). Harmonic analysis of total electron contents time series: Methodology and results. *GPS Solutions, 16*(1), 77–88. https://doi.org/10.1007/s10291-011-0208-x

Artru, J., Farges, T., & Lognonné, P. (2004). Acoustic waves generated from seismic surface waves: Propagation properties determined from doppler sounding observations and normal-mode modelling. *Geophysical Journal International, 158*(3), 1067–1077. https://doi.org/10.1111/j.1365-246X.2004.02377.x

Astafyeva, E. (2019). Ionospheric detection of natural hazards. *Reviews of Geophysics, 57*, 1265–1288. https://doi.org/10.1029/2019rg000668

Astafyeva, E., Maletckii, B., Mikesell, T. D., Munaibari, E., Ravanelli, M., Coisson, P., Manta, F., & Rolland, L. (2022). The 15 January 2022 Hunga Tonga eruption history as inferred from ionospheric observations. *Geophysical Research Letters, 49*(10), e2022GL0988827. https://doi.org/10.1029/2022GL098827

Azeem, I., Yue, J., Hoffmann, L., Miller, S. D., Straka, W. C., & Crowley, G. (2015). Multisensor profiling of a concentric gravity wave event propagating from the troposphere to the ionosphere. *Geophysical Research Letters, 42*, 7874–7880. https://doi.org/10.1002/2015GL065903

Breus, T. K., Krymskii, A. M., Crider, D. H., Ness, N. F., Hinson, D., & Barashyan, K. K. (2004). Effect of the solar radiation in the topside atmosphere/ionosphere of mars: Mars global surveyor observations. *Journal of Geophysical Research: Space Physics*. https://doi.org/10.1029/2004JA010431

Cahyadi, M. N., Handoko, E. Y., Rahayu, R. W., & Heki, K. (2021). Comparison of volcanic explosions in Japan using impulsive ionospheric disturbances. *Earth, Planets and Space, 73*(1), 228. https://doi.org/10.1186/s40623-021-01539-5

Cahyadi, M. N., & Heki, K. (2015). Coseismic ionospheric disturbance of the large strike-slip earthquakes in north Sumatra in 2012: Mw dependence of the disturbance amplitudes. *Geophysical Journal International, 200*(1), 116–129. https://doi.org/10.1093/gji/ggu343

Calais, E., Bernard Minster, J., Hofton, M. A., & Hedlin, M. A. H. (1998). Ionospheric signature of surface mine blasts from global positioning system measurements. *Geophysical Journal International, 132*, 191–202.

Chen, J., Zhang, X., Ren, X., Zhang, J., Freeshah, M., & Zhao, Z. (2020). Ionospheric disturbances detected during a typhoon based on GNSS phase observations: A case study for typhoon Mangkhut over Hong Kong. *Advances in Space Research*. https://doi.org/10.1016/j.asr.2020.06.006. in press.

Chernogor, L. F., & Garmash, K. P. (2021). Physical effects in the atmosphere and geospace accompanying the surface explosion in the city of Beirut on August 4, 2020: Observational data. *Kinematics and Physics of Celestial Bodies 37*, 183–192. https://doi.org/10.3103/S0884591321040036

Ciraolo, L., Azpilicueta, F., Brunini, C., Meza, A., & Radicella, S. M. (2007). Calibration errors on experimental slant total electron content (TEC) determined with GPS. *Journal of Geodesy, 81*(2), 111–120. https://doi.org/10.1007/s00190-006-0093-1

Cullington, A. L. (1958). A man-made or artifcial aurora. *Nature, 182*(4646), 1365–1366.

Dautermann, T., Calais, E., & Mattioli, G. S. (2009). 'Global positioning system detection and energy estimation of the ionospheric wave caused by the 13 july 2003 explosion of the Soufrie're Hills Volcano Montserrat.' *Journal of Geophysical Research.* https://doi.org/10.1029/2008JB005722

Fitzgerald, T. J. (1997). Observations of total electron content perturbations on gps signals caused by a ground level explosion. *Journal of Atmospheric and Solar-Terrestrial Physics, 59*(7), 829–834. https://doi.org/10.1016/s1364-6826(96)00105-8

Fitzgerald, T. J., & Carlos, R. C. (1997). Effects of 450-Kg surface explosions on HF radio reflection from the E layer. *Radio Science, 32*(1), 169–180. https://doi.org/10.1029/96RS02989

Freeshah, M. (2021). Ionospheric disturbances investigation by using ground-based gnss observations from dense CORS. Wuahn University. https://www.researchgate.net/publication/354309888_Ionospheric_Disturbances_Investigation_by_Using_Ground-based_GNSS_Observations_from_Dense_CORS

Freeshah, M., Osama, N., & Zhang, X. (2023). Using real GNSS data for ionospheric disturbance remote sensing associated with strong thunderstorm over Wuhan City. *Acta Geodaetica Et Geophysica*. https://doi.org/10.1007/s40328-023-00423-w

Freeshah, M., Zhang, X., Chen, J., Zhao, Z., Osama, N., Sadek, M., Twumasi, N., & Twumasi, N. (2020a). Detecting ionospheric TEC disturbances by three methods of detrending through dense CORS during a strong thunderstorm. *Annals of Geophysics, 63*(6), 667. https://doi.org/10.4401/ag-8372

Freeshah, M., Zhang, X., & Ren, X. (2020). Using interquartile range to detect TEC perturbations associated with a tropical cyclone crossing through the South China Sea. In *Proceedings of the intercontinental geoinformation days (IGD), Mersin, Turkey, 25–26 November 2020*, 28–31.

Freeshah, M., Zhang, X., Şentürk, E., Adil, M. A., Mousa, B. G., Tariq, A., Ren, X., & Refaat, M. (2021b). Analysis of atmospheric and ionospheric variations due to impacts of super typhoon Mangkhut (1822) in the Northwest Pacific Ocean. *Remote Sensing, 13*(4), 661. https://doi.org/10.3390/rs13040661

Freeshah, M., Zhang, X., Şentürk, E., Ren, X., Adil, M. A., & Xu, G. (2021). Could the Beirut explosion perturb the ionosphere? Pre-results using TEC-GNSS observations. In . F. Ehsan, G. Andreas, S. Michael, S. Benedikt, & X. Chao (Eds.) *EGU General Assembly 2021*, EGU21-8990. online: EGU General Assembly 2021. https://doi.org/10.5194/egusphere-egu21-8990.

Hargreaves, J. K. 1992. *The Solar-Terrestrial Environment*. Cambridge Press.

Hofmann-Wellenhof, B., Lichtenegger, H., & Collins, J. (1992). *Global positioning system theory and practice* (1st ed.). Springer.

Jain, S., Vijay, S. K., & Gwal, A. K. (1996). An empirical model for IEC over lunping. *Advances in Space Research, 18*(6), 263–266. https://doi.org/10.1016/0273-1177(95)00935-3

Jonah, O. F., Coster, A., Zhang, S., Goncharenko, L., Erickson, P. J., de Paula, E. R., & Kherani, E. A. (2018). TID observations and source analysis during the 2017 memorial day weekend

geomagnetic storm over North America. *Journal of Geophysical Research: Space Physics*. https://doi.org/10.1029/2018JA025367

Jonah, O. F., Vergados, P., Krishnamoorthy, S., & Komjathy, A. (2021). Investigating the the ionospheric perturbation following the Beirut explosion event. *Radio Science, 56*(10), e2021RS007302. https://doi.org/10.1029/2021rs007302

Knížová, K., Petra, J. L., Kouba, D., Mošna, Z., Podolská, K., Potužníková, K., Šindelářová, T., Chum, J., & Rusz, J. (2021). Ionosphere influenced from lower-lying atmospheric regions. *Frontiers in Astronomy and Space Sciences*. https://doi.org/10.3389/fspas.2021.651445

Komjathy, A., Yang, Y.-M., Meng, X., Verkhoglyadova, O., Mannucci, A. J., & Langley, R. B. (2016). Review and perspectives: Understanding natural-hazards-generated ionospheric perturbations using GPS measurements and coupled modeling. *Radio Science, 51*, 951–961. https://doi.org/10.1002/2015RS005910

Krasnov, V. M., & Drobzheva, Y. V. (2005). The acoustic field in the ionosphere caused by an underground nuclear explosion. *Journal of Atmospheric and Solar-Terrestrial Physics, 67*(10), 913–920. https://doi.org/10.1016/j.jastp.2005.02.014

Kundu, B., Senapati, B., Matsushita, A., & Heki, K. (2021). Atmospheric wave energy of the 2020 August 4 explosion in Beirut, Lebanon, from ionospheric disturbances. *Scientific Reports*. https://doi.org/10.1038/s41598-021-82355-5

Kurtuluş, H., Livaoğlu, E., Yavuz, T. S., Sertçelik, F., Irmak, C., & Sertçelik, İ. (2018). Seismic characterization of the blast occured in Istanbul (Turkey) by the end of 2016. *Disaster Science and Engineering, 4*(1), 46–53.

Kutiev, I., Tsagouri, I., Perrone, L., Pancheva, D., Mukhtarov, P., Mikhailov, A., Lastovicka, J., et al. (2013). Solar activity impact on the Earth's upper atmosphere. *Journal of Space Weather and Space Climate, 3*, A06. https://doi.org/10.1051/swsc/2013028

Latter, A. L., LeLevier, R. E., Martinelli, E. A., & McMillan, W. G. (1961). A method of concealing underground nuclear explosions. *Journal of Geophysical Research, 66*, 943–946.

Leitinger, R. (1996). Ionospheric electron content. In W. Dieminger, G. K. Hartmann, & R. Leitinger (Eds.), *The upper atmosphere-data analysis and interpretation.* Springer. https://doi.org/10.1007/978-3-642-78717-1

Li, Z., Yuan, Y., Fan, L., Huo, X., & Hsu, H. (2013). Determination of the differential code bias for current BDS satellites. *IEEE Transactions on Geoscience and Remote Sensing, 52*(7), 3968–3979. https://doi.org/10.1109/TGRS.2013.2278545

Mannucci, A. J., Wilson, B. D., Yuan, D. N., Ho, C. H., Lindqwister, U. J., & Runge, T. F. (1998). A global mapping technique for GPS derived ionospheric total electron content measurements. *Radio Science, 33*(3), 565–582.

Meng, X., Vergados, P., Komjathy, A., & Verkhoglyadova, O. (2019). Upper atmospheric responses to surface disturbances: An observational perspective. *Radio Science*. https://doi.org/10.1029/2019rs006858

Mohannakumar, K. (2008). *Stratosphere troposphere interaction: An introduction* (1st ed.). Springer Netherlands. https://doi.org/10.1007/978-1-4020-8217-7

News, BBC. (2020). Russian captain recalls journey that led to deadly cargo being impounded. Archived from the Original on 4 February 2021. Retrieved 19 October 2021'. *News, BBC*. https://www.bbc.com/news/world-middle-east-53683082. Accessed 19 Oct 2020

Panda, D., Senapati, B., Tyagi, B., & Kundu, B. (2019). Effects of Rayleigh–Taylor instability and ionospheric plasma bubbles on the global navigation satellite system signal. *Journal of Asian Earth Sciences, 170*, 225–233. https://doi.org/10.1016/j.jseaes.2018.11.006

Park, J., Von Frese, R. R. B., Grejner-Brzezinska, D. A., Morton, Y., & Gaya-Pique, L. R. (2011a). Ionospheric detection of the 25 May 2009 North Korean underground nuclear test. *Geophysical Research Letters, 38*(L22802), 1–6. https://doi.org/10.1029/2011GL049430

Pilger, C., Gaebler, P., Hupe, P., Kalia, A. C., Schneider, F. M., Steinberg, A., Sudhaus, H., & Ceranna, L. (2021). Yield estimation of the 2020 Beirut explosion using open access waveform and remote sensing data. *Scientific Reports, 11*(1), 14144. https://doi.org/10.1038/s41598-021-93690-y

Ren, X., Chen, J., Li, X., & Zhang, X. (2020a). Ionospheric total electron content estimation using GNSS carrier phase observations based on zero-difference integer ambiguity: Methodology and assessment. *IEEE Transactions on Geoscience and Remote Sensing*. https://doi.org/10.1109/tgrs.2020.2989131

Ren, X., Chen, J., Li, X., & Zhang, X. (2020b). Multi-GNSS contributions to differential code biases determination and regional ionospheric modeling in China. *Advances in Space Research, 65*(1), 221–234. https://doi.org/10.1016/j.asr.2019.10.014

Ren, X., Zhang, J., Chen, J., & Zhang, X. (2021). Global ionospheric modeling using multi-GNSS and upcoming LEO constellations: Two methods and comparison. *IEEE Transactions on Geoscience and Remote Sensing*. https://doi.org/10.1109/TGRS.2021.3050413

Ren, X., Zhang, X., Xie, W., Zhang, K., Yuan, Y., & Li, X. (2016). Global ionospheric modelling using multi-GNSS: BeiDou, Galileo, GLONASS and GPS. *Scientific Reports, 6*(33499), 1–11. https://doi.org/10.1038/srep33499

Rolland, L. M., Lognonné, P., & Munekane, H. (2011). Detection and modeling of Rayleigh wave induced patterns in the ionosphere. *Journal of Geophysical Research: Space Physics*. https://doi.org/10.1029/2010JA016060

Roueff, A., Chanussot, J., & Mars, J. I. (2004). Use of time-scale representations for the analysis of seismic signals. In *SPIE optics east* (pp. 226–37).

Rudenko, G. V., & Uralov, A. M. (1995). Calculation of ionospheric effects due to acoustic radiation from an underground nuclear explosion. *Journal of Atmospheric and Terrestrial Physics, 57*(3), 225–236. https://doi.org/10.1016/0021-9169(93)E0003-R

Salem, M. A., Liu, N., & Rassoul, H. K. (2015). Effects of small thundercloud electrostatic fields on the ionospheric density profile. *Geophysical Research Letters, 42*(6), 1619–1625. https://doi.org/10.1002/2015GL063268

Saqib, M., Adil, M. A., & Freeshah, M. (2023). Pre-earthquake ionospheric perturbation analysis using deep learning techniques. *Advances in Geomatics, 1*(1), 48–67. https://doi.org/10.5281/zenodo.10202326.

Savastano, G., Komjathy, A., Verkhoglyadova, O., Mazzoni, A., Crespi, M., Wei, Y., & Mannucci, A. J. (2017). Real-time detection of tsunami ionospheric disturbances with a stand-alone GNSS receiver: A preliminary feasibility demonstration. *Scientific Reports, 7*, 1–10. https://doi.org/10.1038/srep46607

Savitzky, A., & Golay, M. J. E. (1964). Smoothing and differentiation of data by simplified least squares procedures. *Analytical Chemistry, 36*, 1627–1639. https://doi.org/10.1021/ac60214a047

Schafer, R. W. (2011). What is a savitzky-golay filter? *IEEE Signal Processing Magazine, 28*, 111–117. https://doi.org/10.1109/MSP.2011.941097

Schunk, R. W., & Sojka, J. J. (1997). Global ionosphere-polar wind system during changing magnetic activity. *Journal of Geophysical Research: Space Physics, 102*(A6), 11625–11651. https://doi.org/10.1029/97JA00292

Şentürk, E., Adil, M. A., & Saqib, M. (2021). Ionospheric total electron content response to annular solar eclipse on June 21, 2020. *Advances in Space Research, 67*(6), 1937–1947. https://doi.org/10.1016/j.asr.2020.12.024

Sojka, J. J., Raitt, W. J., & Schunk, R. W. (1981). Theoretical predictions for ion composition in the high-latitude winter F-region for solar minimum and low magnetic activity. *Journal of Geophysical Research, 86*(A4), 2206. https://doi.org/10.1029/ja086ia04p02206

Standard, Evening. (2020). Beirut explosion "One of the largest non-nuclear blasts in history". Retrieved 19 October 2021. https://www.standard.co.uk/news/world/beirut-explosion-one-of-largest-blasts-history-a4517646.html. Accessed 5 Aug 2020

Tang, L., Li, Z., & Zhou, B. (2018). Large-area tsunami signatures in ionosphere observed by GPS TEC after the 2011 Tohoku Earthquake. *GPS Solutions*. https://doi.org/10.1007/s10291-018-0759-1

Vadas, S. L., & Fritts, D. C. (2009). Reconstruction of the gravity wave field from convective plumes via ray tracing. *Annales Geophysicae, 27*(1), 147–177. https://doi.org/10.5194/angeo-27-147-2009

Vergados, P., Komjathy, A., & Meng, X. (2020). GNSS observation for detection, monitoring, and forecasting natural and man-made hazardous events. In *Position, navigation, and timing technologies in the 21st century: Integrated satellite navigation, sensor systems and civil applications* (pp. 939–969). https://doi.org/10.1002/9781119458449.ch32.

Wang, C., Rosen, I. C., Tsurutani, B. T., Verkhoglyadova, O. P., Meng, X., & Mannucci, A. J. (2016). Statistical characterization of ionosphere anomalies and their relationship to space weather events. *Journal of Space Weather and Space Climate, 6*(A5). https://doi.org/10.1051/swsc/2015046.

Webb, H., & Daniels, F. B. (1964). Ionospheric oscillations following a nuclear explosion. *Journal of Geophysical Research, 69*, 545–546. https://doi.org/10.1029/JZ069i003p00545

Yu, B., Xue, X., Gaopeng, L., Ma, M., Dou, X., Qie, X., Ning, B., Lianhuan, H., Jianfei, W., & Chi, Y. (2015). Evidence for lightning-associated enhancement of the ionospheric sporadic E layer dependent on lightning stroke energy. *Journal of Geophysical Research: Space Physics*. https://doi.org/10.1002/2015JA021575.Received

Zhang, X., Guo, F., & Zhou, P. (2014). Improved precise point positioning in the presence of ionospheric scintillation. *GPS Solutions, 18*, 51–60. https://doi.org/10.1007/s10291-012-0309-1.

Zhang, X., & Tang, L. (2015a). Traveling ionospheric disturbances triggered by the 2009 North Korean underground nuclear explosion. *Annales Geophysicae, 33*(1), 137–142. https://doi.org/10.5194/angeo-33-137-2015

Zhang, X., & Tang, L. (2015b). Detection of ionospheric disturbances driven by the 2014 Chile Tsunami using GPS total electron content in New Zealand. *Journal of Geophysics Research: Space Physics, 120*, 1–8. https://doi.org/10.1002/2014JA020879.Received

(Received May 23, 2023, revised October 26, 2023, accepted November 7, 2023)